Source Expansion Nodal Kernel for Multi-Group Pin-by-Pin SP3 Core Calculation

Hyunsik Hong and Han Gyu Joo*
Department of Nuclear Engineering, Seoul National University,
1 Gwanak-ro, Gwanak-gu, Seoul, 08826 Korea
**Corresponding author: joohan@snu.ac.kr*

1. Introduction

The rapid growth in computing power of the present times is notably aided by the heterogeneous parallelization framework employing General Purpose Graphics Processing Units (GPGPUs). The reactor physics laboratory of Seoul National University (SNURPL) has been utilizing GPGPUs in direct whole core calculations through the method of characteristics (MOC) based code nTRACER and also through a continuous energy Monte Carlo code PRAGMA. The GPGPU version of nTRACER can perform a half three-dimensional (3D) hot-zero-power (HZP) core calculation within 4 minutes [1] and PRAGMA can yield nearly 15 time speedup over a CPU-based MC code[2].

Motivated by these successes, SNURPL had considered utilizing GPGPUs in the advanced pin-level two-step core calculation through a multigroup (MG) pin-by-pin simplified P3 (SP3) code SPHINCS [3]. It was, however, noted that the finite difference method (FDM) employing pin size meshes suffers considerable discretization error [4] while it requires the computing resources suitable for CPU-based parallelization [5]. In this regard, the development of a pin-wise nodal kernel for the GPU-based SP3 core calculation was initiated.

The paper presents preliminary study results for the theoretical part of the development. The nodal kernel is in the one-node formulation because of its inherent parallelism and is based on the source expansion nodal method (SENM) [6] to facilitate steep gradients of the higher order flux moment. The discretization error of the SP3 SENM kernel was assessed by the pin-by-pin calculations for the VERA [7] fuel assemblies (FAs).

2. One-Node SP3 Source Expansion Nodal Kernel

The SP3 SENM equation was previously derived [8] but it was considered less appropriate for the pin-wise nodal kernel due to computing burden and complexity of the similarity transformation. Instead, each of the moment equation was decoupled by arranging the off-diagonal reaction terms [3] to the sources in the right-hand-side (RHS) and the surface partial moments were approximated [9, 10] to ease the formulation.

2.1 Formulation of the SP3 SENM Equation

The SP3 equation can be written for the summed flux and the 2nd moment terms as:

$$-D_{0,g}\nabla^2\hat{\phi}_{0,g}+\Sigma_{r0,g}\hat{\phi}_{0,g}=s_{0,g} \tag{1}$$

$$-D_{2,g}\nabla^2\phi_{2,g}+\Sigma_{r2,g}\phi_{2,g}=s_{2,g} \tag{2}$$

where

$$\hat{\phi}_{0,g}=\phi_{0,g}+2\phi_{2,g},$$
$$D_{0,g}=1/(3\Sigma_{tr,g}),\quad D_{2,g}=3/(7\Sigma_{t,g}),$$
$$\Sigma_{r0,g}=\Sigma_{r,g},\quad \Sigma_{r2,g}=\tfrac{4}{3}\Sigma_{r,g}+\tfrac{5}{3}\Sigma_{t,g},$$
$$q_{0,g}=\frac{\chi_g}{k_{eff}}\sum_{g'=1}\nu\Sigma_{f,g'}\phi_{0,g'}+\sum_{g'\neq g}\Sigma_{g'\to g}\phi_{0,g'},$$
$$s_{0,g}=q_{0,g}+2\Sigma_{r,g}\phi_{2,g},\quad s_{2,g}=-\tfrac{2}{3}q_{0,g}+\tfrac{2}{3}\Sigma_{r,g}\hat{\phi}_{0,g}.$$

It would be worthwhile to note that not the 0th moment but the summed flux is added to the 2nd moment source term for stability of the higher moment calculation.

Hereinafter, only the summed flux equation would be discussed since Eq. (1) and (2) share the same form. By applying the transverse integration to Eq. (1) for the *u*-direction and normalizing it for the coordinate variable ξ_u defined in [-1, 1], the equation is written as:

$$\left(-\frac{4D_0}{h_u^2}\frac{d^2}{d\xi_u^2}+\Sigma_r\right)\hat{\phi}_0(\xi_u)=s_0(\xi_u)-L(\xi_u) \tag{3}$$

where the h_u is the node width and the L denotes the transverse leakage externally given as the quadratic polynomial. The group index g was omitted for brevity. In the SENM, the entire RHS of Eq. (3) is approximated by the N-th order polynomial as:

$$Q(\xi_u)=s_0(\xi_u)-L(\xi_u)=\sum_{i=0}^{N}q_{0,i}^u P_i(\xi_u) \tag{4}$$

and Legendre polynomials are employed for the basis. The N is 2 for the pin-and 4 for the assembly-size node because the higher order source expansion is beneficial in accuracy for the large node but severely degenerates the stability for the small node. Hence, the source is expanded by the quadratic in the radial and the quartic in the axial direction for the 3D calculation.

The source expansion coefficient ($q_{0,i}$) is used to determine the analytic solution of Eq. (3) given as:

$$\begin{aligned}\hat{\phi}_0(\xi_u)&=\hat{\phi}_0^H(\xi_u)+\hat{\phi}_0^P(\xi_u)\\&=A_0^u\sinh(\kappa_0^u\xi_u)+B_0^u\cosh(\kappa_0^u\xi_u)+\sum_{i=0}^{N}c_{0,i}^u P_i(\xi_u)\\&=\underline{\hat{\phi}_0}+A_0^u\sinh(\kappa_0^u\xi_u)\\&\quad+B_0^u\left(\cosh(\kappa_0^u\xi_u)-\frac{\sinh(\kappa_0^u)}{\kappa_0^u}\right)+\sum_{i=1}^{N}c_{0,i}^u P_i(\xi_u)\end{aligned} \tag{5}$$

The superscript H and P denote the homogeneous and particular solutions, and

$$\underline{\hat{\phi}}_0 = \tfrac{1}{2}\int_{-1}^{1}\hat{\phi}_0(\xi_u)d\xi_u,$$
$$\kappa_0^u = \tfrac{h_u}{2}\sqrt{\tfrac{\Sigma_{r0}}{D_0}}, \quad \kappa_0^2 = \tfrac{h_u}{2}\sqrt{\tfrac{\Sigma_{r2}}{D_2}}.$$

The particular solution coefficients ($c_{0,i}$) are obtained by the method of undetermined coefficients as:

$$\begin{aligned} c_{0,1} &= \tfrac{1}{\Sigma_{r0}}\left(q_{0,1} + \tfrac{15}{\kappa_0^2}q_{0,3}\right), \quad c_{0,3} = \tfrac{1}{\Sigma_{r0}}q_{0,3}, \\ c_{0,2} &= \tfrac{1}{\Sigma_{r0}}\left(q_{0,2} + \tfrac{35}{\kappa_0^2}q_{0,4}\right), \quad c_{0,4} = \tfrac{1}{\Sigma_{r0}}q_{0,4}. \end{aligned} \tag{6}$$

The u is omitted in Eq. (6) for simplicity. The $c_{0,0}$ is not determined by the $q_{0,i}$ because the node-averaged moments are considered as unknown.

Once the homogeneous and particular solutions are obtained, the $q_{0,i}$ can be determined by the polynomial approximation of Eq. (5):

$$\hat{\phi}_0(\xi_u) \cong \underline{\hat{\phi}}_0 + \sum_{i=1}^{N} a_{0,i}^u P_i(\xi_u) \tag{7}$$

and the coefficient $a_{0,i}$ is obtained by using the orthogonal property of Legendre polynomials. The method and results are detailed in Ref. [6].

2.2 Approximation of the Surface Partial Moments

The homogeneous solution coefficients are determined by using the partial moments defined in terms of the even moments at surface and the net odd moment:

$$\begin{aligned} J_1^{\pm} &= \tfrac{1}{4}\hat{\phi}_0^s \pm \tfrac{1}{2}J_1 - \tfrac{3}{16}\phi_2^s \\ J_3^{\pm} &= \tfrac{7}{16}\phi_2^s \pm \tfrac{1}{2}J_3 - \tfrac{1}{16}\hat{\phi}_0^s \end{aligned} \tag{8}$$

The 2nd moment in the partial 1st moment equation and the summed flux in the partial 3rd moment make difficulty in formulation. For this reason, likewise the approximation in Ref. [10], Eq. (8) is truncated as:

$$\tilde{J}_1^{\pm} = \tfrac{1}{4}\hat{\phi}_0^s \pm \tfrac{1}{2}J_1, \quad \tilde{J}_3^{\pm} = \tfrac{7}{16}\phi_2^s \pm \tfrac{1}{2}J_3 \tag{9}$$

It would be called as the approximated partial moment, contrast to the exact form in Eq. (8). Note that both Eq. (8) and (9) yield the same net moment as:

$$\begin{aligned} J_1 &= -D_0\nabla\hat{\phi}_0 = J_1^+ - J_1^- = \tilde{J}_1^+ - \tilde{J}_1^- \\ J_3 &= -D_2\nabla\phi_2 = J_3^+ - J_3^- = \tilde{J}_3^+ - \tilde{J}_3^- \end{aligned} \tag{10}$$

and their incoming at the reflective boundary is the same with the outgoing. Nonetheless, it should be aware that the vacuum boundary condition arises difference. For the boundary where the real incoming moments are zero, the approximated moments are [10]:

$$\tilde{J}_1^- = \tfrac{3}{109}(\tilde{J}_1^+ + 8\tilde{J}_3^+), \quad \tilde{J}_3^- = \tfrac{1}{109}(14\tilde{J}_1^+ + 3\tilde{J}_3^+) \tag{11}$$

In Eq. (9), fraction of the surface even moment can be an arbitrary number and its selection has negligible effect on the converged solution. Therefore, the homogeneous coefficient A and B for either the summed flux or the 2nd moment ϕ is derived for the fraction μ.

The approximated incoming partial moment at the right and left node boundaries are:

$$\tilde{J}_{in}^r = \mu\phi(1) - \tfrac{1}{2}J(1), \quad \tilde{J}_{in}^l = \mu\phi(-1) + \tfrac{1}{2}J(-1) \tag{12}$$

and the net surface moment is presented as:

$$\begin{aligned} J &= -\frac{2D}{h}\frac{d}{d\xi}\phi(\xi) \\ &= -2\beta k\left(A\cosh(\kappa\xi) + B\sinh(\kappa\xi)\right) + J^P(\xi) \end{aligned} \tag{13}$$

where

$$J^P(\xi) = -\frac{2D}{h}\frac{d}{d\xi}\phi^P(\xi) = -2\beta\sum_{i=1}^{N} c_i P_i'(\xi).$$

By inserting the boundary condition of Eq. (12) in Eq. (13), the homogeneous coefficients are:

$$\begin{aligned} A &= \frac{\tfrac{1}{2}(\tilde{J}_{in}^r - \tilde{J}_{in}^l) - (\mu+\beta)c_1 - (\mu+6\beta)c_3}{\beta k\cosh(\kappa) + \mu\sinh(\kappa)} \\ B &= \frac{-\mu\bar{\phi} + \tfrac{1}{2}(\tilde{J}_{in}^r + \tilde{J}_{in}^l) - (\mu+3\beta)c_2 - (\mu+10\beta)c_4}{\beta\kappa\sinh(\kappa) + \mu\left(\cosh(\kappa) - \sinh(\kappa)/\kappa\right)} \end{aligned} \tag{14}$$

It should be noted that the c_3 and c_4 are zero for the radial direction. The A can be readily determined by the given incoming moments and the particular solution coefficients. On the contrary, the node average moment must be obtained beforehand to determine the B.

By using Eq. (13), the multidimensional nodal balance equation can be written as:

$$\sum_{u=x,y,z}\frac{J_u(1) - J_u(-1)}{h_u} + \Sigma_r\bar{\phi} = \bar{s} \tag{15}$$

with

$$\left(J_u(1) - J_u(-1)\right)/h_u = -\Sigma_D^u\left(\kappa^u\sinh(\kappa^u)B + 3c_2^u + 10c_4^u\right),$$
$$\Sigma_D^u \equiv 4\beta/h_u = 4D/h_u^2.$$

Rearrangement of Eq. (15) gives

$$\bar{\phi} = \left(\bar{s} + C_2\right)/C_1 \tag{16}$$

where

$$C_1 = \Sigma_r + \sum_{u=x,y,z}\Sigma_D^u\mu\tau^u,$$

$$C_2 = \sum_{u=x,y,z}\begin{pmatrix}\Sigma_D^u(\tfrac{1}{2}\tau^u(J_{u,in}^l + J_{u,in}^r) \\ +(3-\tau^u(\mu+3\beta^u))c_2^u + (10-\tau^u(\mu+10\beta^u))c_4^u)\end{pmatrix},$$

$$\tau^u = \frac{\kappa^u\cosh(\kappa^u)}{\beta^u\kappa^u\sinh(\kappa^u) + \mu\left(\cosh(\kappa^u) - \sinh(\kappa^u)/\kappa^u\right)}.$$

Finally, the approximated outgoing moments are:

$$\begin{aligned} \begin{bmatrix}\tilde{J}_{out}^r \\ \tilde{J}_{out}^l\end{bmatrix} &= \begin{bmatrix}\mu\phi(1) + \tfrac{1}{2}J(1) \\ \mu\phi(-1) - \tfrac{1}{2}J(-1)\end{bmatrix} \\ &= \begin{bmatrix}\alpha_s & \alpha_c \\ -\alpha_s & \alpha_c\end{bmatrix}\begin{bmatrix}A \\ B\end{bmatrix} \\ &+ \begin{bmatrix}\mu\left(\bar{\phi} + \phi^P(1)\right) + \tfrac{1}{2}J^P(1) \\ \mu\left(\bar{\phi} + \phi^P(-1)\right) - \tfrac{1}{2}J^P(-1)\end{bmatrix} \end{aligned} \tag{17}$$

Here,

$$\alpha_s = -\beta\kappa\cosh(\kappa) + \mu\sinh(\kappa)$$
$$\alpha_c = -\beta\kappa\sinh(\kappa) + \mu\left(\cosh(\kappa) - \sinh(\kappa)/\kappa\right)$$

3. Accuracy of the One-Node SP3 SENM

Two-dimensional FA calculations were performed to assess the spatial discretization error of the SP3 source expansion nodal kernel. The assemblies have the typical Westinghouse 17x17-type lattice feature. The inter-assembly gap is omitted for simplicity. The details are presented in Table I. The ID here indicates the VERA Problem 2 FA where the specifications were taken.

Table I: Fuel assembly descriptions

ID	Enrichment	Descriptions
G	3.1%	24 Ag-In-Cd control rods
H	3.1%	24 B_4C control rods
K	3.6% + 3.1%	Radial zoning + 24 Pyrex
N	3.1%	104 IFBA + 20 WABA
O	3.1%	12 Gadolinia
P	3.1%	24 Gadolinia

The pin-homogenized 8-group constants (GCs) were generated by 47-group nTRACER calculations [11]. The flat-source MOC solver was employed with the transport corrected P0 option and the ray parameters of a 0.01 cm ray spacing and 32 azimuthal and 4 polar angles in the octant solid sphere. The energy boundaries of the condensed group are given in Ref. [4].

The pin-by-pin SP3 calculations were carried out by the FDM and the SENM solvers. The FDM was employed to obtain the very fine-mesh reference solutions. Note that the FDM solutions based on 4,096 (64x64) meshes per pin were regarded as the true. The nodal expansion method (NEM) based on Ref. [9] and [10] was employed for comparison with SENM. All the calculation results do not incorporate the aid of equivalence factors (EFs) in order to observe only the error reduction by mesh refinement. Note that the paper focus only on the reactivity error versus the mesh refinement, because the pin-by-pin nodal solvers are not well optimized yet so presentation of the computational time may cause a misleading, and the error reduction of the assembly-and pin-wise reaction rates was highly similar with that of the reactivity.

Table II: Reactivity error (pcm) of the pin-by-pin solvers

ID	**Ref. k-inf**	FDM			**NEM**	**SENM**
		1x1	2x2	8x8	**1x1**	**1x1**
G	**0.817349**	6350.3	2399.1	200.6	**141.8**	**138.9**
H	**0.748805**	9020.7	3430.2	288.2	**219.7**	**216.0**
K	**1.008013**	1863.4	668.3	53.3	**30.0**	**29.2**
N	**0.862269**	1370.0	461.6	35.0	**8.4**	**7.7**
O	**1.032027**	2035.5	827.5	75.8	**31.7**	**29.5**
P	**0.900619**	4647.9	1900.6	176.2	**89.4**	**84.3**

Table II presents the reactivity error. Due to the significantly heterogeneous configurations including the control rods and burnable absorbers, the FDM yielded severe discretization error. In case of the H, for example, the error was about 9,021 pcm with the 1x1 and 3,430 pcm with the 2x2 meshes. On the other hand, the nodal methods successfully reduced the error. Although each pin was treated as a mesh, the error of NEM and SENM was about 220 pcm and 216 pcm for the H. The nodal solutions were even better than the FDM 8x8 mesh solutions regardless of the cases.

The error reduction of G and H by the mesh refinement are presented in Fig. 1. The pin sub-meshes were increased up to the 32x32 for the FDM and the 4x4 for the nodal. The results confirmed that the agreement of nodal solvers was maintained in the fine mesh. In conclusion, it can be said that the nodal is nearly about 8 times more accurate than the FDM.

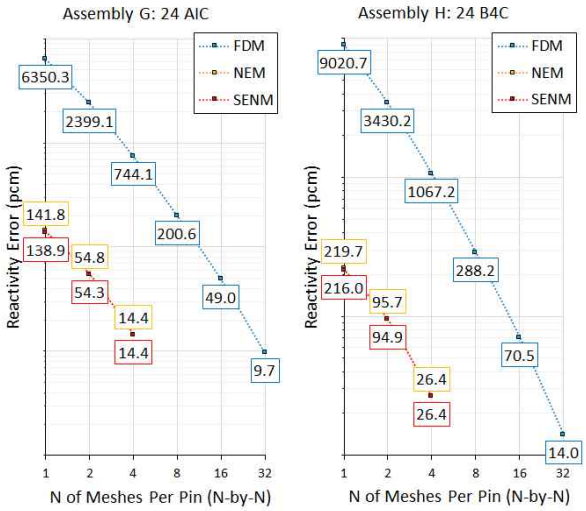

Fig. 1. Reduction of the discretization error by the mesh refinement for the G (left) and H (right) assemblies

It is known that the SENM can yield better accuracy than polynomial-based nodal methods like the NEM, due to the hyperbolic functions employed for the flux expansion. As shown in Table II and Fig. 1, however, the difference between the SENM and the NEM was not notable in the pin-by-pin calculations. Reduction of the source expansion order for the pin-size node was considered as the reason, because it was clear that the quadratic approximation is less accurate than the quartic. Thus, test calculations with the quartic source were performed and the results are in Table III.

In contrast to the assumption, the source expansion order negligibly changed the results while degenerated the stability; the calculations with the 4th order source and the 4x4 meshes together were all diverged. It is because the homogeneous solution coefficients in Eq. (14) are directly determined by the 3rd and 4th order source coefficient in case of the fine-mesh calculation and those are fluctuating until the solution is converged.

Table III: Reactivity error (pcm) of the pin-wise SENM kernel with the different source expansion order

ID	Exp. Ord.	1x1	2x2	4x4
G	2nd	138.9	54.3	14.4
	4th	138.1	54.1	N/A
H	2nd	216.0	94.9	26.4
	4th	215.0	94.7	N/A
K	2nd	29.2	5.7	1.0
	4th	29.0	5.7	N/A
N	2nd	7.7	2.9	0.8
	4th	7.6	2.9	N/A
O	2nd	29.5	14.5	4.4
	4th	28.6	14.3	N/A
P	2nd	84.3	34.6	10.5
	4th	82.3	33.9	N/A

4. Conclusions

The one-node SP3 nodal kernel for the GPU-based pin-by-pin core analysis was formulated in this work. Each of the even moment equation was decoupled by arranging the off-diagonal terms of the matrix equation to the source, and the surface odd moments were approximated to ease the formulation. The order of source expansion in the radial directions was truncated to the 2nd to improve the stability. It was shown that the truncation negligibly changed the solution.

Preliminary test calculations were performed for two-dimensional fuel assemblies based on the VERA BOC HZP fuel lattice configurations. Any of the equivalence factors were not incorporated in the test to observe the reduction of discretization error by the mesh refinement. Accuracy of the SENM was assessed by comparison with the FDM reference solutions based on the very fine-meshes. The test results revealed that the SENM is nearly about 8 times more accurate than the FDM, in terms of the discretization error.

It was also notable that the NEM solutions were very close to the SENM. It means the hyperbolic functions which require significant computing cost might not be much-needed for the radial pin-by-pin flux expansion. Thus, the future work would focus on the NEM vs. SENM comparison for problems with more realistic and challenging features, and the radial NEM and the axial SENM combination which might reduce the computing cost while retaining the accuracy.

ACKNOWLEDGEMENT

This research is supported by the Brain Korea 21 Plus Program (No.21A20130012821).

REFERENCES

[1] N. Choi, J. Kang, H. G. Joo, Preliminary Performance Assessment of GPU Acceleration Module in nTRACER, Trans. of KNS Autumn Meeting, Yeosu, Korea, October 25-26, 2018.
[2] N. Choi, K. M. Kim, H. G. Joo, Initial Development of PRAGMA – A GPU-Based Continuous Energy Monte Carlo Code for Practical Applications, Trans. of KNS Autumn Meeting, Goyang, Korea, October 24-25, 2019.
[3] H. H. Cho, H. G. Joo and et al, Preliminary Development of Simplified P3 based Pin-by-Pin Core Simulator SPHINCS, Trans. of KNS, Jeju, Korea, May 23-24, 2019.
[4] H. Hong and H. G. Joo, Analysis of Error Sources in Pin-Homogenized Multi-Group Calculations, Trans. of KNS, Jeju, Korea, May 21-22, 2020.
[5] J. T. Hwang, N. J. Choi, H. G. Joo, Pin-by-Pin 2D/1D SP3 FDM Scheme with 3D Assembly-wise CMFD Acceleration, Trans. of KNS, Jeju, Korea, May 23-24, 2019.
[6] J. I. Yoon and H. G. Joo, Two-Level Coarse Mesh Finite Difference Formulation with Multigroup Source Expansion Nodal Kernels, J. of Nuc. Sci. Tech., Vol. 45, no. 7, pp. 668-682, 2008.
[7] A. Godfrey, VERA Core Physics Benchmark Progression Problem Specifications, CASL-U-2012-0131-004, Oak Ridge National Laboratory, Consortium for Advanced Simulation of LWRs, Rev. 4, August 29, 2014.
[8] H. J. Jeong, Alternating Direction One-Dimensional Source Expansion Nodal Method for Whole Core Simplified P3 Calculation. M.S. Thesis, Seoul National University, 2013.
[9] C. H. Lee, T. J. Downar, A Hybrid Nodal Diffusion/SP3 Method Using One-Node Coarse-Mesh Finite Difference Formulation, Nuc. Sci. Eng., Vol 146, pp. 176-187, 2004.
[10] T. Downar, Y. Xu, V. Seker, PARCS v3.0 U.S. NRC Core Neutronics Simulator Theory Manual, University of Michigan, December 1, 2009.
[11] Y. S. Jung, H. G. Joo et. al., Practical numerical reactor employing direct whole core neutron transport and subchannel thermal/hydraulic solvers, Ann. Nuc. Energy, Vol. 62, pp. 357-374, 2013.